Wave transformation over a barrier reef

Damien Sous, Marion Tissier, Vincent Rey, Julien Touboul, Frederic Bouchette, Jean-Luc Devenon, Cristele Chevalier, Jerome Aucan

Damien Sous, Marion Tissier, Vincent Rey, Julien Touboul, Frederic Bouchette, et al.. Wave transformation over a barrier reef. Continental Shelf Research, 2019, 10.1016/j.csr.2019.07.010 . hal-02188471

Wave transformation over a barrier reef

Damien Sous [a,b], Marion Tissier [c], Vincent Rey [b], Julien Touboul [b], Frédéric Bouchette [d], Jean-Luc Devenon [e], Cristele Chevalier [e], Jerôme Aucan [f]

[a] *Université de Pau & Pays Adour / E2S UPPA, Laboratoire des Sciences de l'Ingénieur Appliquées la Mécanique et au Génie Electrique (SIAME) - MIRA, EA4581, 64600, Anglet, France*
[b] *Université de Toulon, Aix Marseille Université, CNRS, IRD, Mediterranean Institute of Oceanography (MIO), La Garde, France*
[c] *Environmental Fluid Mechanics Section, Faculty of Civil Engineering and Geosciences, Delft University of Technology, Stevinweg 1, Delft 2628CN, The Netherlands*
[d] *Gosciences-Montpellier, Univ Montpellier, CNRS, Univ Antilles, Montpellier, France*
[e] *Aix Marseille Université, Université de Toulon, CNRS, IRD, Mediterranean Institute of Oceanography (MIO), La Garde, France*
[f] *LEGOS, UMR5566, IRD, Nouméa, France*

Abstract

This paper reports a combined observational and numerical study of wave transformation over barrier reefs. The field instrumentation, which consists in a cross-shore network of pressure sensors and one high resolution velocity profiler, has been deployed for more than two months over the Ouano reef barrier, New Caledonia. The combined analysis of observations and numerical simulations shows that the reef barrier acts as an efficient, but depth-dependent, filter for incoming wave energy. The data analysis reveals the presence of very low frequency standing wave patterns due to reflection either at the reef barrier inner boundary or at the lagoon shore. Another striking feature is the development of undular bore trains over the reef flat.

Keywords: wave transformation; reef barrier; infragravity waves; very low frequency; undular bores; field experiments; shallow water model

---

1. Introduction

Facing now a growing series of threats, the coral reef-lagoon systems have become an important challenges of coastal oceanography. When present, waves play a direct role on the health of the reef colony by inducing mixing, aeration and sediment/nutrient transport. In addition to these direct effects, waves are a significant driver of the lagoon circulation, and thus affect the renewal, quality and richness of lagoon waters [1, 2, 3, 4, 5, 6]. Furthermore, during extreme events such as tropical storms, cyclones or tsunamis, the sheltering role played by the reef can be determining for shore and inland damages such as massive erosion, submersion or flooding [7]. A major issue is to understand how the incoming wave energy is transferred to the shore and to the lagoon. To the first order, the wave transformation across the reef results from the reef topography and roughness, the incoming wave features and the water level [1, 2, 3, 4, 8]. When approaching the forereef, incident waves experience shoaling, refraction, reflection and bottom friction with variable magnitudes depending on the waves and the geometric features of the forereef. On the reef flat, more complex dynamics arise as soon as the incoming wave height is sufficient to induce wave breaking; a wave setup driven by gradients in radiation stresses, turbulent and frictional dissipation and wave/wave harmonic transfers progressively develop. The forereef being steep and complex [9], the wave breaking over a reef barrier is *a priori* expected to show significant differences from that observed on classical sandy beaches [10]. However, recent studies tend to show that the depth-averaged features (setup, radiation stress, wave transport) can be well described by models initially developed for milder slope [11, 12, 13, 14, 15]. The importance of long infragravity (IG) waves in reef environments is now well established by field and numerical studies [11, 16]. In the nearshore, IG waves are usually forced by the groupiness of the incoming gravity short waves (SW), i.e. the time-space modulation of the envelope of swell waves [16, 17, 18]. Along forereef steep slopes, the breaking mechanism is generally expected to dominate the bound wave release in the development of IG waves [16, 11, 17]. A distinction can be made in the low frequency band between IG and very low frequency (VLF) bands. The usual motivation for such distinction is that in the VLF band, free surface fluctuations are mainly controlled by topo-bathymetric features inducing standing seiche-like oscillations. Such VLF motions, potentially resonating, have been identified in fringing reef systems [17, 19, 20].

Most of the reef hydrodynamics studies, involving laboratory, field and/or numerical approaches, have been carried out in the context of fringing reefs [11, 21, 14, 20, 22, 23]. The primary focus is here the functioning of barrier reef systems, for which less data are available [6, 12, 24]. The field site has been selected because it is one of the most archetypal reef barrier system amongst the South Pacific, with a wide, regular and rectilinear reef barrier isolated from the land by a well-developed channel lagoon and exposed to long swells originating from the Southern Ocean and approaching with a nearly reef normal incidence. The approach adopted here is to provide a comprehensive view of the barrier reef wave dynamics using both field measurements and numerical simulations. The present paper focuses on short (SW) and long (IG and VLF) wave transformations over the barrier reef and into the lagoon. The first part of the manuscript is dedicated to the presentation of the observations, including the site and the measurement techniques. The second part describes the field results while additional insights on the studied processes are provided by numerical modelling in the third section. The last section is dedicated to conclusions and prospects.

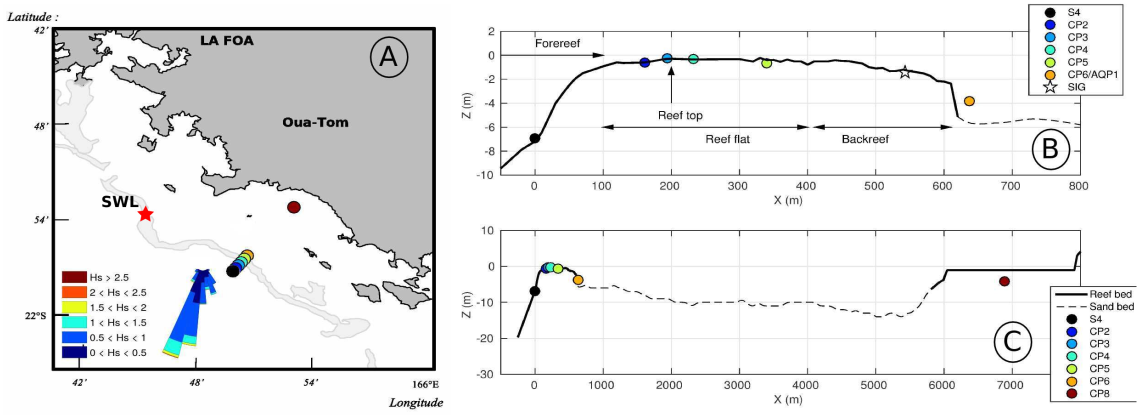

Figure 1: Field site and instrumentation. A: the Ouano reef-lagoon system. For the sake of visual commodity, the marks indicating the sensors are not scaled. The red star denotes the measurement point for the Still Water Level. The directional rose indicates the incoming wave direction statistics. B: a zoomed view of the instrumented cross-reef profile showing the devices deployed on the reef barrier, and C: the same devices (plus the equipment set in the inner lagoon) plotted on a typical cross-reef section at the scale of the entire coastal system.

2. Experiments

2.1. Field site

This work uses a data set from a large hydro-biogeochemical field campaign (OLZO and CROSS-REEF projects) conducted from April to August 2016 in New Caledonia (South Pacific Ocean). The studied site is the Ouano reef-lagoon system (Fig. 1, A), located south-west of the island. It is a weakly anthropized lagoon, nearly 30 km long, 10 km wide and 10 m deep, exposed to micro tides (tidal range 1.7 m) and exposed to remotely-generated Southern Ocean Swells (Fig. 1, A). It can be classified as a channel lagoon [25]. Further details on the general lagoon hydrodynamics are reported in [6, 26, 25].

The instrumentation considered here has been deployed on a single cross-reef transect (see description below and Fig. 1A,C). In the following, the reef barrier (Fig 1B) is decomposed in three main areas that differ in terms of slope and biotic structures: the forereef, the reef flat and the backreef. The forereef is the steepest and most rugged area, with cross-shore spurs and grooves up to 2 to 3 m deep. The reef flat is made of compact coral colonies with typical heights of coral elements ranging between 0.1 and 0.4 m while the backreef is generally covered by smaller coral boulders (0.1-0.2 m) on a dead coral bed with scattered but larger pinnacles (up to 0.6-0.8 m), see Figure 2.

2.2. Measurements and methods

2.2.1. Instrumentation and data

The instrumentation has been designed to study the hydrodynamics of the reef barrier, combining free surface wave and current measurements. Incoming wave conditions over the reef outer slope are provided by a S4 electro-current meter (-7.3 m deep) on the forereef recording 20-min bursts of data at 2 Hz every 3 h. Note that, unfortunately, due to the malfunction of the forereef pressure sensor, free surface fluctuations at S4 are deduced from velocity alone, using linear wave theory. The linear reconstruction of free surface motion from bottom moored sensor requires the

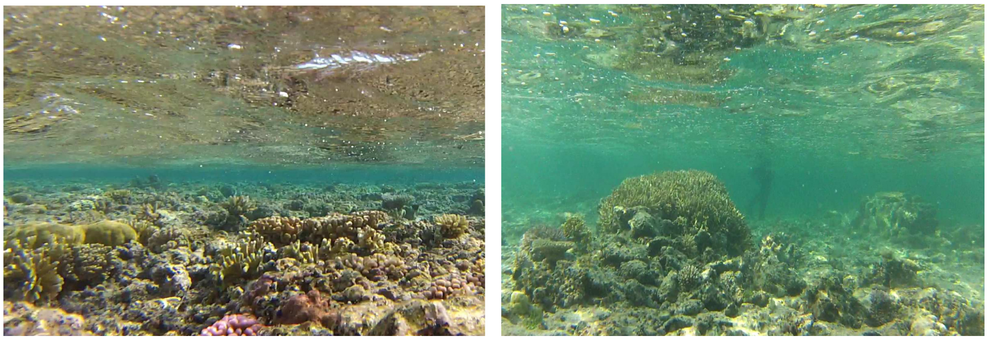

Figure 2: Underwater pictures for reef flat (left) and backreef (right). The typical size of coral elements shown in the pictures is about 0.2 and 0.7 m for reef flat and backreef, respectively.

local wave length to be at least twice the depth. This imposes a high frequency limit for the short wave about 0.33 Hz for the S4 location. For the sake of robustness, only integral and spectral short wave (SW) characteristics will be used in the following analysis. Deep water wave height H_0 is obtained by reverse shoaling of the measured significant wave height using linear theory assuming shore-normal waves. This latter assumption is justified by the typical wave climate at Ouano [25], the occurrence of a steep slope and a very limited refraction over the forereef (see Section 2.2.3). In the following analysis of reef hydrodynamics, the wave forcing is provided by those reverse-shoaled wave conditions from the S4 device.

Six autonomous pressure sensors were deployed at the bottom from the reef top to the inner lagoon (see Fig. 1). The reef flat sensors CP2 to CP5 are OSSI Wave Gauge® sensors recording continuously bottom pressure at 5 Hz while the lagoon pressure sensors CP6 to CP8 are RBR Duo recording at 2 Hz, also in continuous mode. All pressure measurements were first corrected using the atmospheric pressure measured at the Tontouta airport (25 km westward). Free surface elevations were then calculated using linear wave theory. The maximal local depth above the reef flat is nearly 1.7 m such as the short wave limit is about 0.7 Hz for CP2 to CP5 sensors, while it decreases for deeper sensors to about 0.5 and 0.35 Hz for SIG (see below) and CP6, respectively. Energy spectra were computed over 80-min bursts subdivided from the continuous record. For each pressure sensor, a discrete Fourier transform was computed without any windowing to preserve the high frequency resolution. The resulting spectra were then smoothed using a 0.0044 Hz moving average (44 degrees of freedom). The Still Water Level (SWL) data was recovered from an additional pressure sensor located in the northern Isié 1 km-wide reef passage, see the red star in Figure 1.

A high-resolution upward looking Nortek Signature 1000 profiler (SIG) was deployed above the backreef to study the vertical structure and turbulence properties of the cross-reef current. The SIG profiler was positioned in a small depression of the reef colony. The profiler measured the three components of the velocity during 20 min bursts at 4 Hz. The PUV method was used to separate incident and reflected wave components, based on the depth-averaged value of the velocity measured between 0.3 and 0.6 m above the top of the surrounding canopy (10 cells of 3 cm). In addition to the velocity profile, the SIG profiler gives access to the local bottom pressure. The measured velocities were projected into cross and along-reef components using the reef main axes: cross-reef and along reef are heading 30° and 120° clockwise from the North (nautical convention). Positive values of cross-reef and along-reef components correspond to northward (water entering) and westward currents, respectively. The calculation of depth-averaged currents was performed by extending the velocity profile down to the bottom using a parabolic interpolation. Practically, the measured profile is completed by a zero-velocity point at the bottom and a second-order polynomial interpolation is performed to fill the gap between the bottom and the lowest measurement point at the resolution of the measured profile (3 cm). The entire reconstructed profile is then integrated from the bottom up to the free surface.

The wave period discussed later on is described using the classical peak period T_p, which is a relevant parameter for the wave climate in Ouano generally dominated by long swells. For each wave component (SW, IG or VLF), the significant wave height was computed as:

$$H_s = 4\sqrt{\int_{f_{min}}^{f_{max}} E(f)df} \tag{1}$$

where $E(f) = 0.5 \quad S(f)^2$ is the spectral density of energy from discrete Fourier transform spectral estimate $S(f)$ and f_{min} and f_{max} are the frequency limits discussed later on. Following the assumptions of linear wave theory, the wave energy, i.e. the sum of potential and kinetic energies, was computed as $\frac{1}{16}\rho g H_s^2$ with ρ the water density and g the gravity.

2.2.2. Bathymetry and positioning

The acquisition of reliable bathymetric data in reef context, i.e. with very complex three dimensional seafloor structure, is a challenging task, in particular in areas exposed to waves, and, consequently, the definition of the exact depth above the reef barrier remains a difficult issue despite its importance for the study of wave transformation and for the computation of cross-reef transports. The present bathymetric data are provided by the compilation of four in-situ surveys of the reef barrier and the forereef slope, which have then been combined with larger scale lagoon bathymetry from the ZoNéCo atlas [27]. The surveys were performed at high tide during the calmest conditions encountered during the April-July period, in order to go back and forth across the entire reef easily. It should be noted that the different reef compactions observed along the reef flat and backreef areas alter the measurement of bed elevation. In particular, the single beam sounding (Lowrance Hook ® echo sounder) tends to capture the top of the reef canopy in the reef flat area and the dead coral bed in the backreef. To correct for this inconsistency, a 30 cm correction was applied to the reef flat bed elevation. This corresponds to the elevation below which the horizontal velocity was zero, following the method proposed by Monismith et al. [12]. However, this correction was not applied where the echo-sounder provided a good estimate of the bed elevation in the backreef after removal peaks associated to coral pinnacles and protrusions. The resulting noise-filtered and smoothed bathymetric profile, which will be used for numerical modelling, is given in Fig. 1, C. It is emphasized that, due to the agitation encountered even in the most quiet periods selected for the surveys and the complexity of the forereef structure, the measurements performed in the most exposed area (forereef and outer reef flat) should still be considered with caution. Bathymetry and instruments are all related to the local hydrographic datum (EPSG:5151).

When possible, instruments were positioned by DGPS. The backreef sensors (CP4-CP5) positions have been repeatedly measured during spring low tides. They are therefore used as references for correcting the vertical elevation of the deeper sensors. The technique used here relies on the fact that in the absence of waves and currents, the difference of time-averaged elevations between two sensors tends to zero. Thus, for each sensor, the 40-min averaged elevation difference with respect to the reference sensors was plotted versus wave height for the whole time series. If needed, a correction in vertical position elevation was applied to the selected sensor such as the difference tends to zero for zero wave energy. By cross-checking the results provided by the reference sensors, the overall uncertainty on free surface level is estimated at 5 cm.

2.2.3. Overview of the wave forcing and selected events

Figure 3 (A,B,C) shows the wave conditions during the experiments. The overall climate is typical of the South-West coast of New Caledonia, as observed during previous experiments [25]. The Ouano reef is mainly exposed to long South Pacific swell waves, with mean wave height of 1.8 m and mean peak period about 12.5 s, hitting the coast with a nearly reef-normal incidence.

In addition to field measurements, two numerical WW3 outputs are presented, one provided by the 30 second resolution IOWAGA WW3 implementation [28] at point 22° S, 165° 5 E (about 35 km westward), and the other provided by a refined, higher resolution, WW3 implementation on an unstructured grid at 21°57.552'S, 165°50.700'E (about 2 km southward from the studied site). The latter WWIII implementation being forced by the former global model. A very good agreement is observed between forereef measurements and global and local numerical predictions with root mean squared errors of 0.38 and 0.32 m (see also Fig. 3, A-B). This validates the use of velocity only to compute forereef wave features by linear theory. Refraction effects are responsible for the progressive alignment of the wave direction with the shore normal, which is around 210° (nautical convention) at the studied site (Fig. 3, C).

Wind measurements performed at the nearby Tontouta airport station ($\approx$ 30 km) [25] are depicted in Figure 3, D and E. Trade winds are modulated by thermal breeze and guided by the mountainous topography of New Caledonia. The dominant pattern is clear: strong winds always blow from the South-East and almost no winds are coming from the North-West. Daily variations were observed with minimal and offshore winds during nights and a progressive increase and rotation during the day and a decrease in the late afternoon.

A series of events are selected for detailed analysis to highlight the response of barrier hydrodynamics to changes in wave energy and water level. The parameters are listed in Table 1. The reference case, hereinafter named Ref, corresponds to mid tide with a swell of $H_s = 2.5$ m and $T_p = 10.7$ s. A1 and A2 are the closest high and low tides to Ref case. B1 and B2 are high and low tides for the strongest swell event observed. In these cases, the wave height was so large that the forereef S4 measurement was certainly in the breaking zone. The incoming wave height has thus been *a posteriori* reconstructed using SWASH numerical simulations (SW2 configuration). C1 and C2 correspond to fair weather conditions at high and low tide respectively while D1 and D2 have been selected to highlight the effect of variations of the mean wave period.

3. Field Results

3.1. Wave transformation

Compared to the well-known gentle slope sandy beach context, wave transformation over nearshore coral reefs is generally affected by the forereef slope and the strong bottom roughness [4, 5, 16, 11, 12, 24, 29]. To facilitate data interpretation, the distinction is made here between VLF, IG and SW in terms of frequency ranges. The corresponding bands are 0.0004 to 0.01 Hz, 0.01 to 0.04

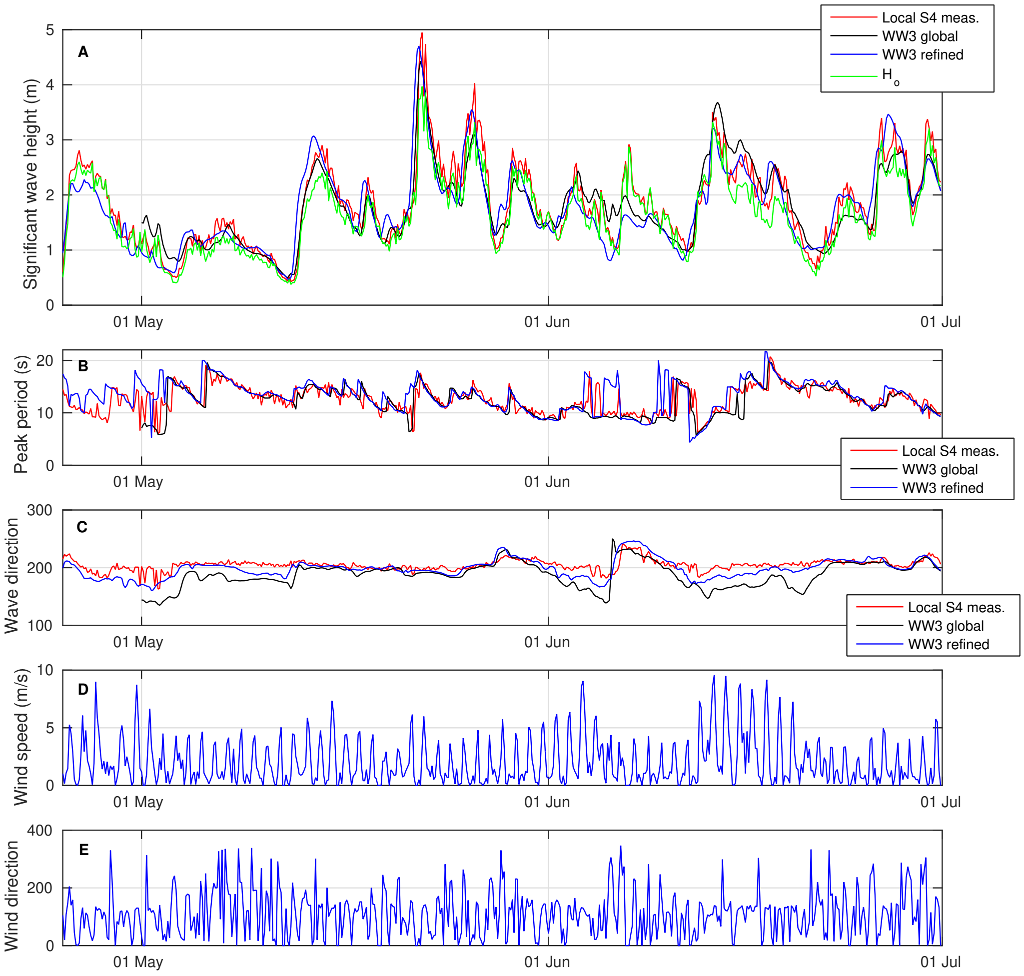

Figure 3: Wave and wind conditions during the field experiments. A: significant wave heights. B: peak periods. C: peak wave direction. D: wind speed. E: wind direction.

CASE	**CONDITIONS**					
	Date	Tide	H_o (m)	T_p (s)	Dir. (^{o})	SWL (m)
Ref	May, 29, 17:40	Mid	2.5	11.4	217	0.27
A1	May, 29, 15:40	High	2.44	11.4	218	0.53
A2	May, 29, 19:40	Low	2.55	10.9	216	-0.06
B1	May, 22, 9:10	High	5.1	16.2	195	0.64
B2	May, 22, 15:10	Low	5.2	15.6	195	0.11
C1	May, 20, 09:10	High	1.1	11.4	195	0.65
C2	May, 20, 03:10	Low	1.3	11.8	203	-0.33
D1	May, 26, 11:00	High	2.72	14.6	205	0.56
D2	May, 26, 8:00	Low	3.1	15	204	-0.04

Table 1: Benchmark cases and corresponding offshore conditions. H_0 is the deshoaled significant deep water wave height (from S4 measurements), T_p the peak period (from the measure at S4), Dir. is the peak wave direction (from WW3 numerical simulations performed on the local grid), SWL is the still water level at Isié reef passage

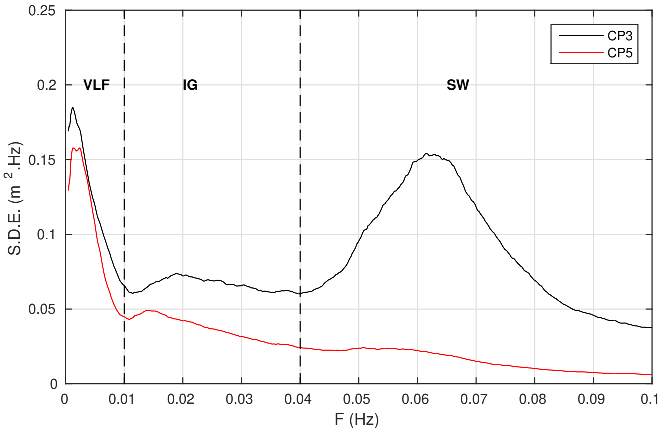

Figure 4: 2-month averaged energy density spectra for CP3 and CP5 sensors. Frequency thresholds are fixed at 0.01 and 0.04 Hz for VLF/IG and IG/SW, respectively

Hz and 0.04 to 0.35 Hz, respectively. Note that the definition of a proper IG/VLF limit is not a straightforward task. Based on two-month averaged spectra measured at CP3 and CP5 (see Fig. 4), the selected value is 0.01 Hz instead of the 0.005 Hz value used previously in reef studies [17, 20]. The reason for this choice is two-fold. First, a local energy minimum is generally observed around this frequency in the measured spectra (see Fig. 5). Furthermore, as highlighted by the following data analysis and the numerical simulations, a major difference is observed in wave dynamics above and below that frequency.

Figure 5 depicts the wave transformation for Ref, A1 and A2 at mid, high and low tides, respectively, while the incoming wave height remains nearly constant. The forereef wave spectrum (Fig. 5, B) shows the presence of several components in the SW band. Looking first at Ref case, one notes the rapid drop of SW height over the forereef under the combined influence of wave breaking, frictional dissipation and energy transfer. Figures 5, D and F, reveal a progressive shift of energy toward lower frequencies in IG and VLF band. At CP2, the incident SW spectral content, initially ranging between 0.08 and 0.12 Hz, is already transformed, shifted toward low frequencies and focused around 0.07 Hz. Both IG and SW show an overall decrease of SW and IG wave heights from CP2 sensor (Fig. 5, C and E). Numerical simulations performed in Section 4.2 show that this trend is mainly due to frictional dissipation. VLF wave heights are also decreasing along the barrier (Fig. 5, E) excepted for A1 high tide case that shows a maximum at CP4. This latter trend is attributed to the presence of standing wave patterns attached to the reef which is further discussed in Section 3.2.

The role of water depth is similar for each wave component: the lower the SWL, the higher the attenuation. The depth also affects the spectral content, with a complete filtering of SW energy over the backreef (CP4 and CP5 in Fig. 5, F) at low tide. At high tide (A1 in Fig. 5, E and F), a moderate amount of SW energy is allowed to pass over the reef crest while the initial incident energy peaks above 0.08 Hz are strongly damped.

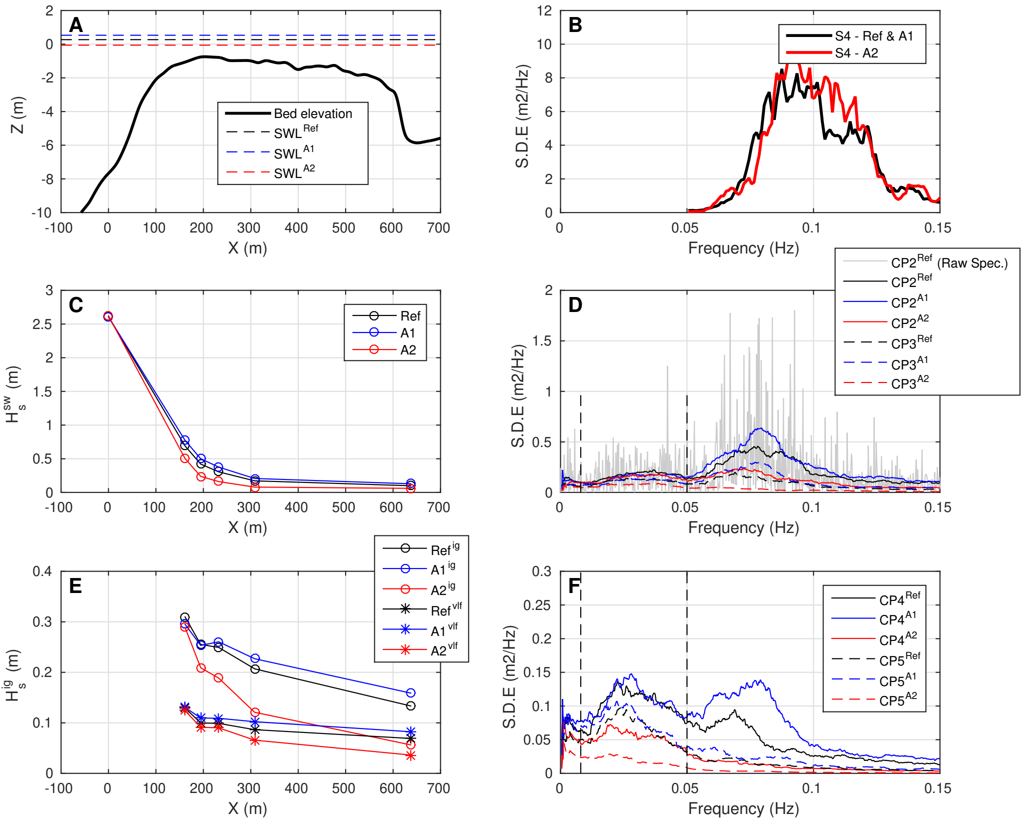

Figure 5: Wave transformation over the reef barrier for cases Ref, A1 and A2. A: Bed elevation and SWL. C and E: cross-shore profiles of SW and IG significant wave heights. B: forereef spectral density of energy (S.D.E.) measured at S4, note that Ref and A1 cases are on the same S4 data burst (20 min burst taken each 3 h). D and F: spectral density of energy for sensors CP2, CP3, CP4, CP5 for Ref, A1 and A2 cases. The Ref raw spectrum is given in D in grey dashed line. The vertical dashed lines in D and F represent the frequency thresholds for VLF and IG.

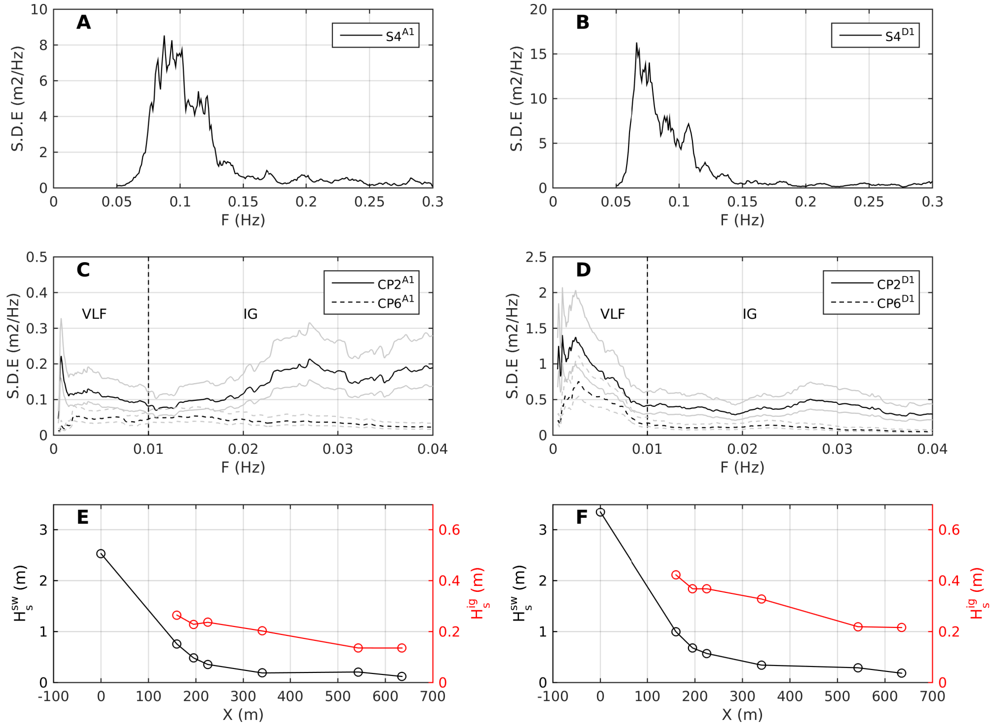

Figure 6: Wave dynamics for cases A1 and D1. A and B: SW spectral density of energy over the forereef for A1 and D1, respectively. C and D: spectral density of energy at CP2 and CP6 for A1 and D1, respectively. Vertical dashed lines in C and D depict the frequency threshold between VLF and IG bands while light grey lines give the 90 % confidence interval. E and F: Cross-shore profiles of SW (black) and IG (red) wave heights for A1 and D1, respectively.

3.2. IG and VLF

The long wave dynamics over the reef barrier for cases A1 and D1 is detailed in Figures 6 and 7, with a particular focus on IG and VLF bands, respectively. The analysis is first performed on the IG content, i.e. in the 0.01 to 0.04 Hz frequency band. Both A1 and D1 are characterized by large waves with comparable deep water wave height ($H_o = 2.44$ and 2.72 m, respectively) but with larger wave periods for D1 ($T_p = 14.6$ s instead of 10.9 s for A1, see S4 forereef spectra in Fig. 6, A and B). The longer wave case is associated to a stronger shoaling before breaking, as highlighted by the larger wave height prior breaking at the forereef (see H_s at $X = 0$ m in Fig 6, E and F). The difference in wave period also induces strong differences in IG spectral content above the reef barrier, which is about 63 % greater for D1 than for A1. A strong IG wave attenuation is observed between the surf zone (CP2) and the barrier end (CP6) with a decrease of the energy content of about 50 % for A1 and D1. The evolution of spectral shapes in Figures 6, E and F, indicates a more pronounced decrease in the upper part of the IG band ($0.025 < f < 0.04$ Hz). Numerical tests performed in Section 4.2 show that the IG damping can be mainly attributed to frictional dissipation.

Figure 7 depicts the VLF dynamics across the barrier for both A1 and D1. Theoretical standing oscillations frequencies for lagoon and reef seiching modes are shown in vertical dashed lines in subfigures C to E (see discussion in Section 5). As observed for IG waves, the longer wave case (D1) produces more VLF waves on the barrier than the short wave case (A1) but the trend is stronger, with significant VLF wave height being about three times greater for D1 than for A1 (Fig. 7, G and H). In case A1, a strong peak is observed around 0.0009 Hz in the surf zone (CP2 in Fig. 7, C) with another weakly defined peak about 0.0035 Hz. At the end of the barrier (CP6 in Fig. 7, C), a much smaller peak is observed at this frequency while the maximal energy is about 0.0021 Hz. At the other side of the lagoon in CP8 (in Fig. 7, E), the stronger energy is again found about 0.0021 Hz while the lower peak at 0.0009 Hz is still well defined. Similar overall trends are observed for D1 combined with a global increase in VLF energy. At CP2, an additional peak is observed about 0.0006 Hz but not found at the other sensors. The second peak observed in A1 at 0.0021 Hz is here stronger above the barrier and slightly shifted about 0.0025 Hz. Spatial modulation of VLF wave amplitude are observed across the barrier, in particular for D1 (Fig. 7, G).

Additional information is obtained from PUV method [30] which is used to separate incident and reflected energies at the SIG profiler for D1, see Figure 8. Strong differences are observed between IG and VLF bands. Significant reflection is measured in the VLF band ($f < 0.01$ Hz), with an averaged wave energy reflection coefficient of 91 %. Three peaks are observed in the incident VLF components, about 0.0009, 0.025 and 0.05 Hz. The two upper peaks are also observed in the reflected component, while the lower peak is no more observed. The reflection is much weaker in the IG band, with a corresponding coefficient about 35 %.

To identify the conditions favourable for the long waves development, Figure 9 depicts the dependency of IG and VLF significant wave heights measured at the reef top (CP3) and in the lagoon (CP6) on the incident short wave offshore energy flux $H_o^2 T_p$ for the entire dataset. The VLF band is here divided in an upper component $0.0017 < f < 0.008$ Hz (superscript *vlfR*, Fig. 9 C and D) and a lower component ($0.0008 < f < 0.0017$ Hz, superscript *vlfL*, Fig. 9 E and F). The color levels indicate the water depth above the reef top. The IG wave height at the reef top is well correlated ($R^2 = 0.7$) with the short wave energy flux (Fig. 9, A), while the depth plays a weak role. At the inner boundary of the reef barrier (CP6, Fig. 9, B), the overall amount of IG energy is weaker. The IG dependency on offshore wave energy flux is still observed ($R^2 = 0.51$) but is now largely modulated by the water depth above the barrier: the lower the water level, the stronger the dissipation and the lower the amount of IG energy. In the VLF band, the overall tendency is again that higher incoming swell energy fluxes lead to more VLF fluctuations. VLF fluctuations are generally greater on the reef top (Fig. 9, C and E) than at the inner barrier boundary (Fig. 9, D and F). A striking difference between upper and lower VLF components is the response to the water depth. The former shows a similar behavior than the IG fluctuations, with higher water levels allowing higher wave energy at the inner barrier boundary while the latter appears much less dependent on the water depth.

3.3. Undular bores

A remarkable observation of in-situ or aerial views (see Fig. 10) of the Ouano reef barrier is the recurring presence of short wave trains propagating across the backreef, nearly from the end of the surf zone up to the end of the barrier. These short waves, firstly identified in the present

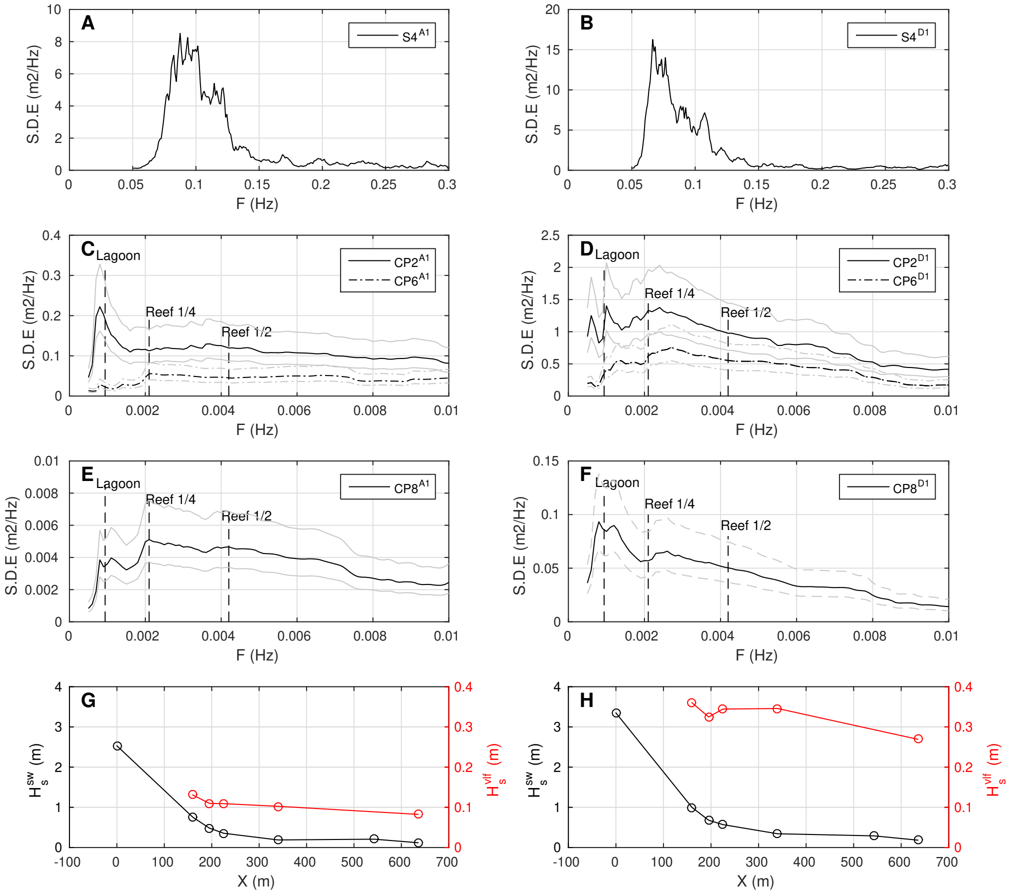

Figure 7: Wave dynamics for cases A1 and D1. A and B: SW spectral density of energy over the forereef for A1 and D1, respectively. C and D: spectral density of energy in the VLF band at CP2 and CP6 for A1 and D1, respectively. E and F: spectral density of energy in the VLF band at CP8 for A1 and D1, respectively. The vertical dashed lines represent the theoretical seiching frequencies for the lagoon fundamental mode and the reef-attached quarter and half wave length (see Section 5). Light grey lines give the 90 % confidence interval. G and H: Cross-shore profiles of SW (black) and VLF (red) wave heights for A1 and D1, respectively.

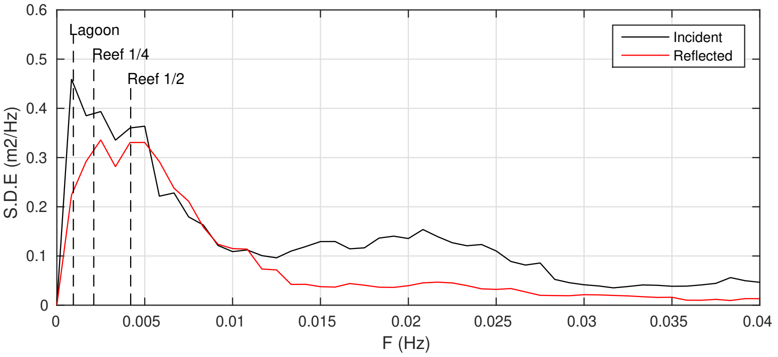

Figure 8: Incident (black) and reflected (red) spectral density of energy for D1 case. The vertical dashed line represent the theoretical seiching frequencies for the lagoon fundamental mode and the reef-attached quarter and half wave length (see Section 5).

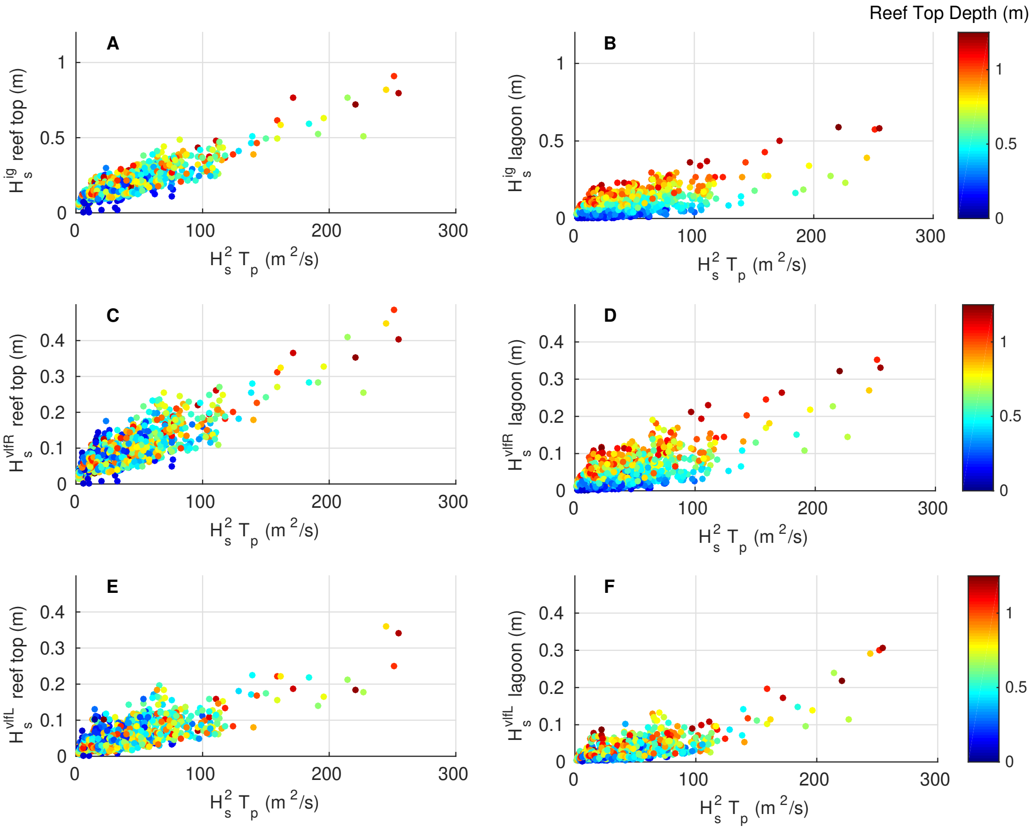

Figure 9: Long wave significant wave height versus deep water short wave energy flux. A and B: IG component for CP3 (reef top) and CP6 (lagoon) sensors. C and D: vlfR reef-attached component for CP3 (reef top) and CP6 (lagoon) sensors. E and F: vlfL lagoon-attached for CP3 (reef top) and CP6 (lagoon) sensors. Reef top depth is indicated by color levels.

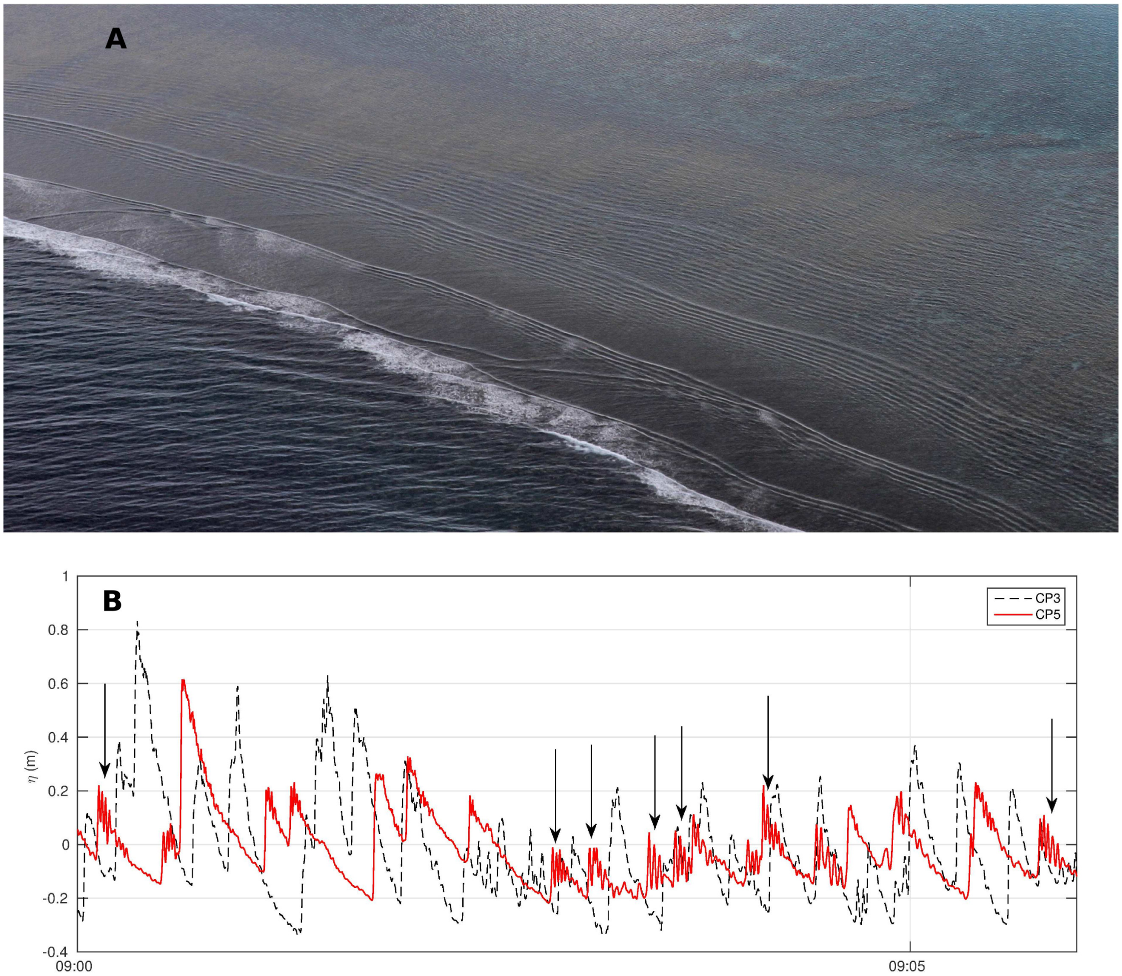

Figure 10: A: aerial view of undular bores over the Ouano barrier reef. B: onset conditions of undular bores over the backreef: time series of free surface elevation computed from two bottom pressure measurement for reef top (CP3) and backreef (CP5) sensors. Black arrows are used to highlight the development of undular bores trains.

site by Chevalier et al. [6], can be described as propagating undular bores or "whelps" [32]. Often discussed in the long wave or tsunami context, the growth of these short waves, or undulations, is the result of the departure from hydrostatic distribution near the steep wave front [33, 34, 35]. The train of undulations progressively grows behind the wave front and remains standing relatively to the leading wave front, similar to what is observed for undular hydraulic jumps [32].

Figure 10, A, compares 5-min free surface elevation time series at the reef top (CP3, black dashed line) and over the back reef (CP5, red solid line) during the same time period. This means that individual waves recorded at CP3 are passing above CP5 few tens of seconds later, depending on the local depth. The onset of undulations at the front of the remaining swell waves is clearly related to the depth and wave height. A Froude number can be estimated for each individual wave front, roughly considered here as a hydraulic jump, using the upstream (d_1) and downstream depths

(d_2) (see [32]):

$$F_r = \sqrt{\frac{1}{8}\left(\left(2\frac{d_2}{d_1}+1\right)^2 - 1\right)} \tag{2}$$

Such Froude number has been computed for each individual wave over a 20-min time period that includes the time series shown in Fig. 10. For each individual wave, the upstream depth d_1 is measured as the minimal depth at the toe of the wave while the downstream depth d_2 is the depth at the following wave crest which is averaged over the two first undulations when an undular bore is present. The undular bores are observed to develop for Froude number lower than about 1.45. This value can be compared with observations of undular hydraulic jumps gathered by Chanson [32]. While a wide spread exists between experiments, undular jumps were observed to develop for $F_r > 1$, and disappear for $1.5 < F_r < 3$. In the present case, for Froude numbers larger than about 1.45, the wave front looks rather like a classical asymmetric inner surf zone breaking wave. It is remarkable that, even if their onset conditions are expected to be rather restrictive [32], the Ouano's backreef appears to be often in a favourable range of water depths, wave heights and currents all along the tidal cycle. The low-frequency modulation of the water depth induced by the long waves across the reef also seems to play an important role in undular bore development. Broken swell waves propagating on the long wave crest at CP3 (see first waves Fig. 10, dashed line) dissipate their energy at a lower rate due to the increased water depth than the waves propagating on the long wave trough. As a result, they are able to keep a higher height $(d_2 - d_1)$ and thus a higher Froude number at CP5. They therefore mostly exhibit a classical saw-tooth shape at CP5. On the other hand, broken swell waves that propagate in a reduced water depth (long wave trough) at CP5 see their Froude number significantly decreasing between the sensors, leading to the onset of undular bores. Thus the development of undulations is controlled by the local current and depth conditions which are driven by external forcing (tidal cycle, wave energy and other large scale processes) but also constantly modulated by the presence of IG/VLF waves over the barrier.

A time-frequency analysis on a 150 s selected event is performed in Fig. 11, A, using Morlet wavelets. The development of undular bores is associated to energy transfers from the swell range of SW ($0.04 < f < 0.35$ Hz) to higher frequencies. The amount of wave energy carried by such whelps is of interest. A time evolution of the energy distribution between SW ($0.04 < f < 0.35$ Hz) and undular bores ($0.35 < f < 1$ Hz) is thus computed for the selected event using a 10 s sliding window. The ratio of energy contained in the undular bore and the SW frequency ranges is computed as

$$\frac{\int_{0.35}^{0.7} E(f)df}{\int_{0.04}^{0.35} E(f)df} \tag{3}$$

where $E(f)$ is the spectral density of energy. Note that linear theory is again used to give a first estimate of total wave energy (i.e. potential and kinetic) from pressure measurement alone as no velocity measurements were available at this location. This ratio is plotted in Fig. 11, B. It appears that, despite their striking visual signature, these trains of undulations only capture a weak part of the SW energy with a maximum about 3 % which represents 1.7 % in terms of significant wave height.

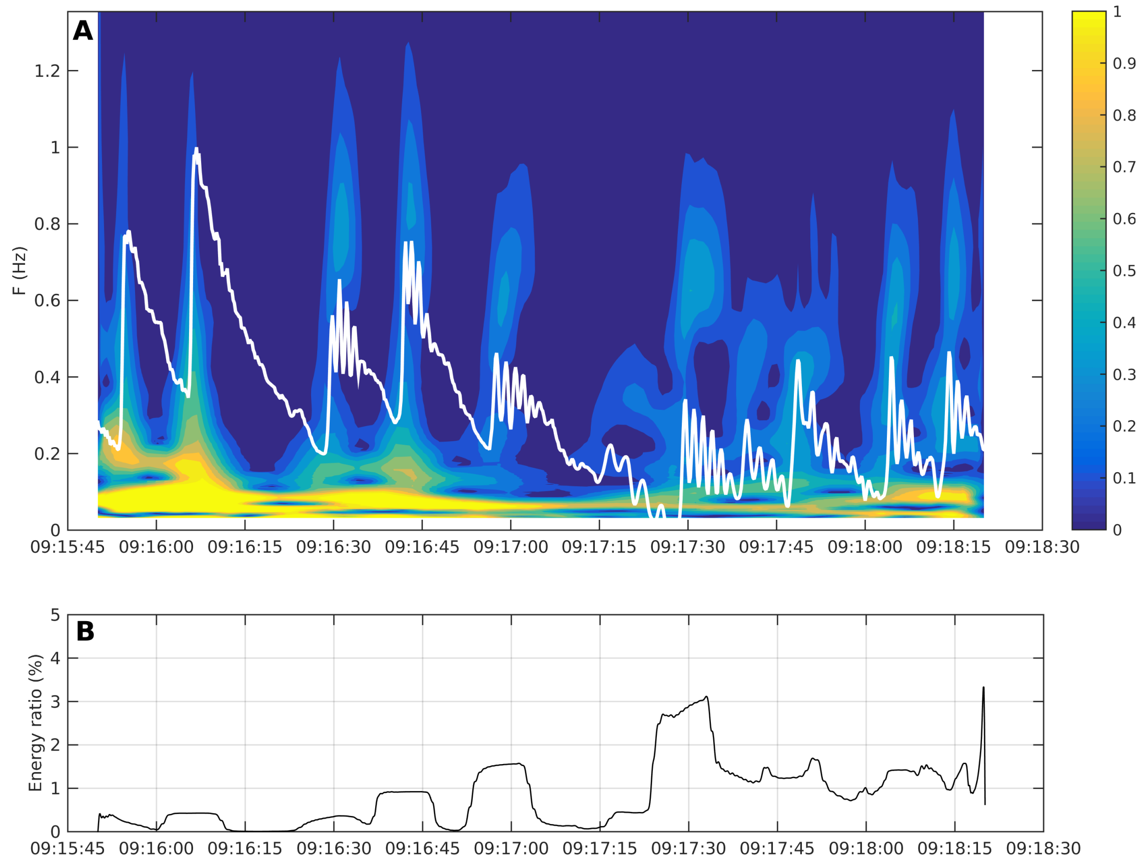

Figure 11: A: time-frequency analysis for a selected period. The color code depicts the envelope of energy density (in m^2/Hz) computed from wavelet analysis. The white line indicates the normalized free surface elevation. B: time evolution of the wave energy ratio between undular bores ($0.35 < f < 1$Hz) and SW ($0.04 < f < 0.35$Hz).

4. Numerical modelling

Several strategies have been used to model the hydrodynamics above coral reefs. At the scale of reef-lagoon systems, the most commonly used approaches involve strict spectral models such as SWAN [36, 37] or short-wave averaged and infragravity-wave resolving models such as XBeach [16, 11, 38]. Although originally designed for gentle slope and smooth bottom environments, these models have been successfully applied to wave transformation on fringing reefs, including IG wave generation, through a simple adjustment of the friction constant [11]. Finer details on fringing reefs hydrodynamics, both in the laboratory and in the field, have been obtained from phase-resolving simulations using non-hydrostatic models such as SWASH [39, 38, 40] or Boussinesq-type models [14, 15].

In the following, selected events from the present field dataset are compared with the numerical predictions provided by the open-source short wave-resolving SWASH model [41]. The numerical model is first introduced (Section 4.1) and compared to field data (Section 4.2) to assess to which extent it is able to describe wave transformation and momentum balance above the reef. Additional simulations are then carried out to gain further insight on VLF motions (Section 4.3) and undular bores (Section 4.4).

4.1. Model setup

The phase-resolving model SWASH is used with two different vertical resolutions, using respectively two and ten vertical terrain-following layers (called respectively SW2 and SW10 in the following). The model is first tested and calibrated against the cross-shore evolution of wave height measured on May, 29, around mid tide, which is the reference case, and then used to simulate the series of cases listed in Table 1.

The model is forced by a synthetic time series built from a Jonswap spectrum based on the measured wave period T_p. The incoming significant wave height was estimated in the previous section from linear reverse-shoaling of the measurements at S4. Second-order bound infragravity waves are added at the offshore boundary of the model based on weakly non-linear finite-depth wave theory [42, 43]. For a quantitative comparison between measurements and model outputs, a more accurate description of the offshore wave forcing would have been needed. However, due to the harshness of the forereef area, only one instrument deployment (S4) was achieved, which limits the knowledge of wave transformation from deep water to the breaking point. As the present analysis is focused on wave breaking and transformation across the barrier, the approach retained here is, for each case, to *a posteriori* slightly adjust the incoming wave height such as the model predictions fit the S4 measurements. This adjusted wave height H_a, used for the numerical simulations, is also indicated in Table 2 and compared to the deshoaled S4 wave height H_o.

For each numerical case, a 30-min wave run is performed on the same cross-shore profile, within a 2.5 km long domain ($-250 < X < 2000$ m) with 1 m of horizontal resolution. For $X > -10$ m, the measured water depth is used, while for $-500 < X < -10$ m, a linear slope is assumed based on the available nautical charts. The offshore boundary of the domain, at $X = -500$ m, is 30 m deep. The measured mean water levels are imposed at each boundary such as the simulated current accounts for both the wave-induced current above the reef and the across-reef surface-gradient related current due to tidal oscillations and other large scale features.

The model parameters are adjusted to get the best fit simultaneously on SW height and mean water level (MWL) profiles for the reference case. All model parameters are kept to default values except those mentioned here. The depth-dependent Manning formulation is used for the friction coefficient, with a spatially constant value. For SW2, the only calibrated parameter is the Manning coefficient which is fixed at 0.06 s.m$^{-1/3}$ adjusted on SW and MWL profiles. The use of more layers requires to increase the Manning coefficient (0.1 s.m$^{-1/3}$) and to use a background turbulent viscosity (0.003 m^2/s). The breaking parameter α is used in SWASH for the 2 layer configuration to initiate breaking, while it is no more required when using a sufficient vertical resolution (here 10 layers for SW10). Previous numerical studies on fringing reefs indicate that the later breaking observed on steep slopes should be taken into account by increasing α [38] but this effect is expected to be compensated, with an unknown magnitude, by roughness effects [44]. For the sake of simplicity, the breaking parameter is therefore kept to default value ($\alpha = 0.6$) in the present study. A 500m wide sponge layer is finally imposed at the lagoon boundary.

An additional case, named SW2b, has been performed to test the effect of friction on wave transformation. This case is similar to SW2, except that a 0.01 Manning coefficient is used on the reef flat for $X > 100$ m, that is to say a value 6 times smaller than for SW2.

4.2. Wave transformation

Let us first focus on Ref case on which the different model configurations have been calibrated. Figure 12 depicts the cross-shore evolution of measured and predicted SW significant wave height, IG significant wave height and MWL. It can be seen that, after a proper calibration, each configuration provides a fair overall description of the SW transformation across the reef barrier (see also Table 2). Before the breaking point, both configurations show the same behavior, with a weak shoaling-induced wave amplification and small modulations of the wave envelope mainly due to weak wave reflection over the forereef (about 1 % in wave energy). The breaking point location is very similar whether a breaking parameter is used (SW2) or not (SW10). A strong decrease in SW energy is then predicted by both models. The numerical prediction of IG wave dynamics is generally less consistent with field measurements than for SW on which the model is calibrated. The global trend is an overestimation of the IG wave magnitude over the reef flat (between 21 and 31 % , see Table 2). The overestimation of IG waves can be partly compensated by increasing the friction parameter, but this strongly undermines the overall momentum balance, and therefore the MWL. This suggests an excessive IG production above the forereef, which may be related to inadequacies in the wave forcing (see also Section 5), inaccuracies in the bathymetric survey and/or the effect of bottom friction. This latter is accounted for in the models by a spatially constant friction coefficient. Such simple approach is certainly not able to represent the very large roughness on the forereef, which is frequently broken by 2-3 m deep trenches. However, due to the lack of more precise in-situ information on wave transformation in this area, the numerical representation of friction is kept as simple as possible, i.e. spatially constant.

The comparison between SW2 and SW2b (reduced friction on the reef flat) demonstrates the effect of frictional dissipation on both IG and SW dynamics on the reef flat. The effect is particularly significant for IG waves, which highlights the predominance of bottom friction in the decrease of IG wave height across the reef barrier compared to other processes such as energy transfer or deshoaling. For the rest of the numerical analysis, the SW2 configuration is used because it provides the best

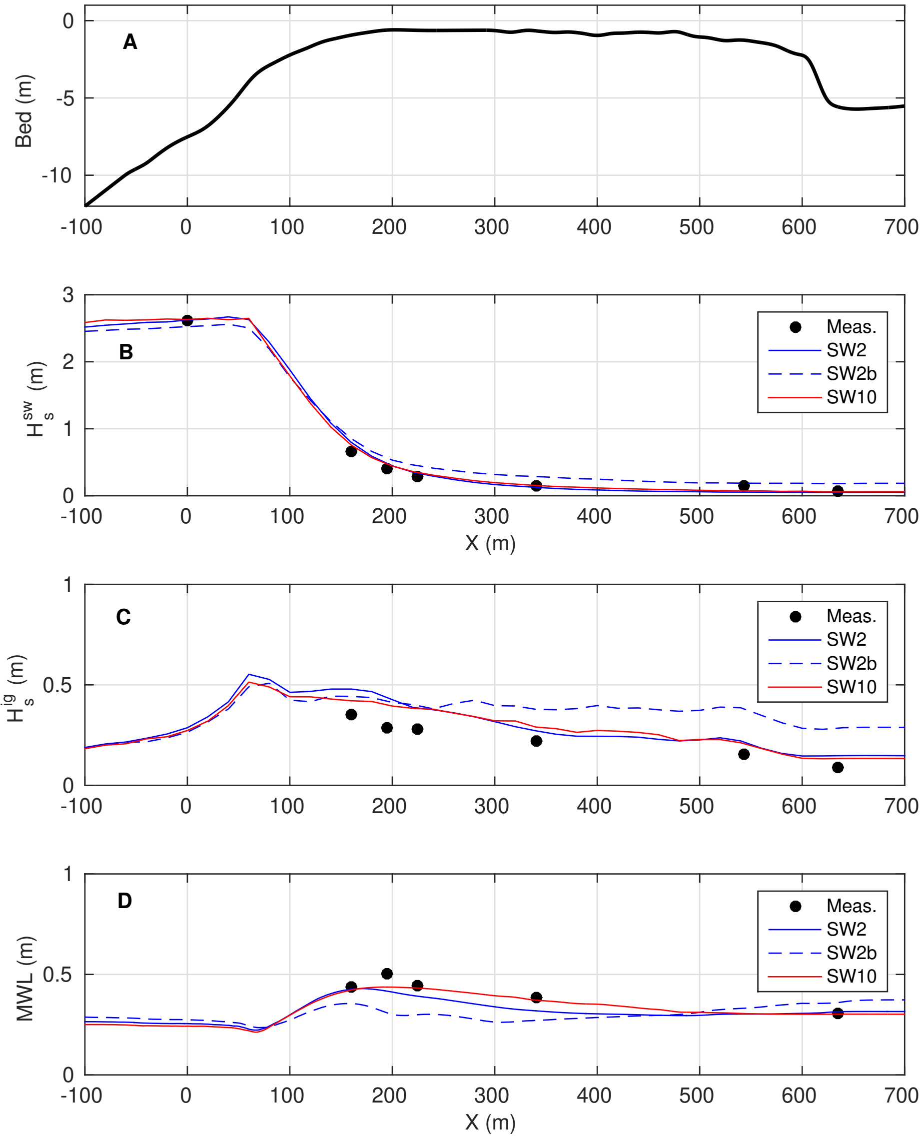

Figure 12: Cross-shore reef wave transformation with comparison between field measurements (black dots) and model predictions for SW2, SW2b (reduced friction on the reef flat) and SW10 configurations. A: bathymetric profile. B: SW significant wave height. C: IG significant wave height. D: MWL. Note that the entire computational domain is not represented here.

compromise between accuracy and computational time.

Several lessons can be drawn for the series of additional SW2 test cases listed in Table 1. The comparisons with field measurements are summarised in Table 2. It can be seen that the model is not able to represent accurately the effect of water level on the reef hydrodynamics. This is for instance highlighted by comparing Ref, A1 and A2 for which wave forcing is nearly steady (see Table 1, $H_a = 2.4$ m) and the tide is mid, high and low with still water levels at 0.27, 0.53 and -0.06 m respectively. More specifically, the model tends to over/underestimate the wave height over the reef at low/high tide. For instance, average relative errors on SW height for CP2, CP3 and CP4 sensors are 3.2 and -10 % for low and high tides, respectively. This observation is attributed to the inability of the Manning formulation to represent the depth-dependency of friction processes. This feature, and the above-mentioned fact that IG waves tend to be overestimated, are exacerbated when increasing incoming wave energy (cases B1 and B2 in Tab. 2). Apart from that, the model is able to provide a very good representation of the wave dynamics across the barrier. Further investigations will be performed to provide a better parameterization of the bottom friction.

4.3. VLF

The present analysis of field data highlights the presence of VLF patterns above the reef barrier, in particular during high wave energy conditions. The respective contributions of barrier and/or boundaries to the development of standing wave structure is further explored using numerical simulations on three partially idealised test cases with SW2 configuration (see Fig. 13). The three cases are based on the complete cross-shore profile of the reef-lagoon system from X=-500 to 8000 m and are performed with the same wave forcing (H_s=3 m and T_p=16 s). They only differ by the water depth and the onshore boundary conditions:

- the Rigid Boundary case (hereinafter RB) is based on the complete bathymetric profile shown in Figure 1 modified by a rigid vertical wall at the shore at $X = 8000$ m;
- the Absorbing Boundary case (hereinafter AB) is similar to the RB case up to $X = 5500$ m, with an open Sommerfeld radiation boundary condition at the shore (see Fig. 13);
- the Continuous Reef case (hereinafter CR) has a extended reef flat, with a constant depth of 1 m up to the shore and a Sommerfeld condition (see Fig. 13).

Figure 14 shows the incident and reflected energy spectra computed over the reef (for RB, AB and CR) separated with the PUV method [30] using the model outputs above the reef ($X = 400$ m). Let us first focus on RB case, which is the case the most representative of the real reef-lagoon system. Two main energy peaks are observed in the incident component, the first in the IG band around 0.012 Hz and the second in the VLF band around 0.004 Hz. A third lower peak is present at lower frequency around 0.0009 Hz. The reflected spectra show negligible reflection above 0.007 Hz. Below this threshold, a significant reflection is observed, in particular for the 0.0009 Hz peak for which most of the wave energy is reflected. Imposing an absorbing boundary at the shore (AB case, in red in Fig. 14) drastically reduces the reflected energy around 0.0009 Hz while significant reflection is still present for the band 0.002 - 0.006 Hz. For the CR case, in which the bathymetric step at the inner reef barrier boundary is removed, the reflection is very weak for the entire spectrum.

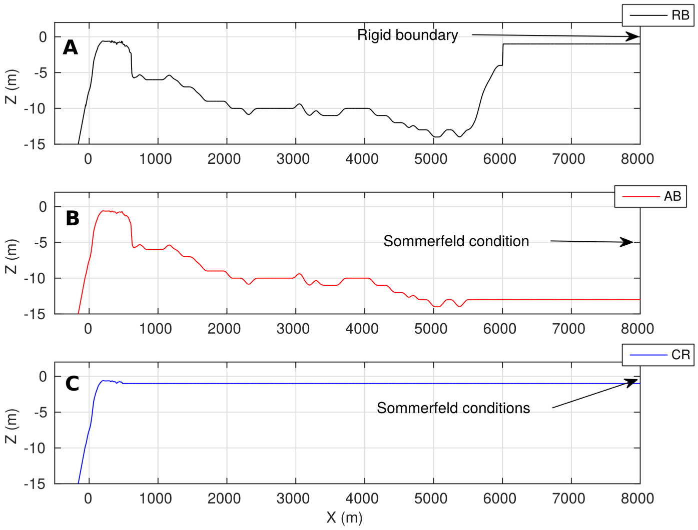

Figure 13: Bathymetry and onshore boundary conditions for the three idealised cases RB (Rigid Boundary), AB (Absorbing Boundary) and CR (Continuous Reef).

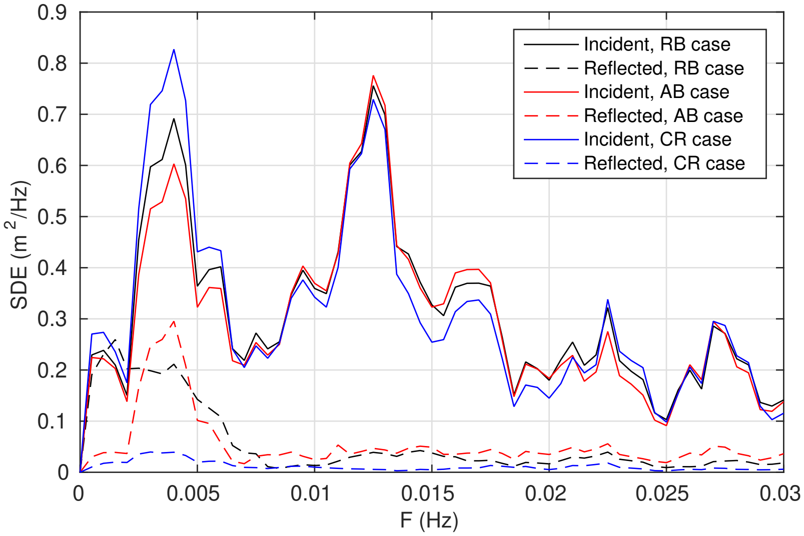

Figure 14: Incident (solid lines) and reflected (dashed lines) spectral densities of energy for the three idealized numerical cases RB, AB and CR.

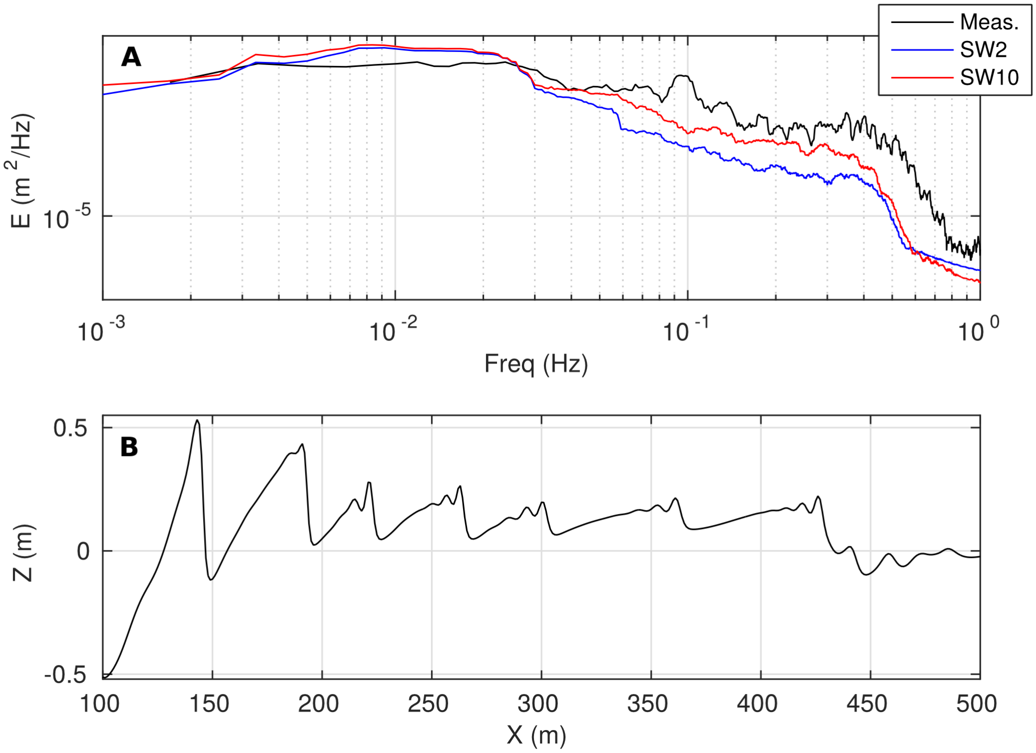

Figure 15: Undular bore formation from SWASH model. A: compared energy density spectra at the SIG measurement point from measurement (black), SW2 (blue) and SW10 (red). B: illustrative profile of free surface elevation across the reef barrier from SW10 showing the transformation of SW fronts into undular bores.

4.4. Undular bores

The field measurements revealed the development of undular bore trains over the barrier. The question arises on their ability to propagate further onshore and to contribute to wave agitation within the lagoon. In order to explore this issue with the numerical model, the first step is to test the ability of SWASH to represent such high frequency wave trains. Both SW2 and SW10 model configurations have been tested. As the model is forced by statistical wave parameters (see discussion above), the comparison against field measurements is performed in terms of overall free surface shape (Fig. 15, B, for SW10 only) and energy spectra (Fig. 15, A, for SW2 and SW10). The model is, at least qualitatively, able to reproduce the destabilization of the incoming wave front in a series of small undulations. However, one notes two significant differences with the measured free surface shape depicted in Figure 11. First, the amplitude of the undulations is much smaller, i.e. of the order of a few centimeters for the model instead of 10 to 20 cm for the measurements. Second, the undulations are shorter and much more numerous for the field case. Such an observation is confirmed on the energy spectra shown in Figure 15, A. The high frequency energy content in the undular bore range ($f > 0.3$ Hz) is underestimated by both model configurations. Despite such discrepancy between model and measurements, the numerical model has been further used to better understand the bore dynamics after passing the barrier. Figure 16, A, shows a snapshot example of the predicted free surface elevation across the transition from the barrier to the lagoon. One notes first the perturbations induced by the bathymetric step at the barrier end (vertical dashed line) and the evolution of the free surface toward an IG-dominated state within the lagoon. While locally affected by the depth threshold when entering the lagoon, the undular bore trains propagate within the lagoon and progressively increase in wave length. As discussed previously, the conditions of propagation of undular bores are greatly controlled by the local height of the water column. The depth-modulating role played by IG/VLF waves on bore dynamics deserves further dedicated analyses, which are out of the scope of the present study. It may however be noted that, as shown by Fig. 16 (B), the undular bores can contribute to a non-negligible portion of the short wave agitation within the lagoon (up to 40 % of the SW significant height in the simulated cases) and, as such, should be accounted for when analyzing the mobilization of sediments, nutrients and larvae in the reef-lagoon system. This numerical result cannot be directly compared with data in the present experimental setup, as bottom-moored pressure sensors in the lagoon are too deep to provide an accurate estimate of such short-crested wave (see Section 2.2.1 for a discussion on the high-frequency limit for CP6).

5. Discussion

Despite some limitations inherent to the harshness of in-situ instrumentation of reef barriers exposed to waves, which will be further discussed, the present study confirmed existing observations and revealed some important additional features of wave transformation over barrier reefs. The incoming swell waves are subject to a range of processes such as the energy in the gravity band is considerably reduced within the lagoon and become nearly negligible in most cases. Each of the involved processes are depth-dependent: the lower the water level is, the weaker the remaining SW energy in the lagoon.

When reaching the forereef, incoming swell waves are first refracted and reflected. Although rather weak in the typical wave climate at the Ouano reef, the former mechanism can be high-

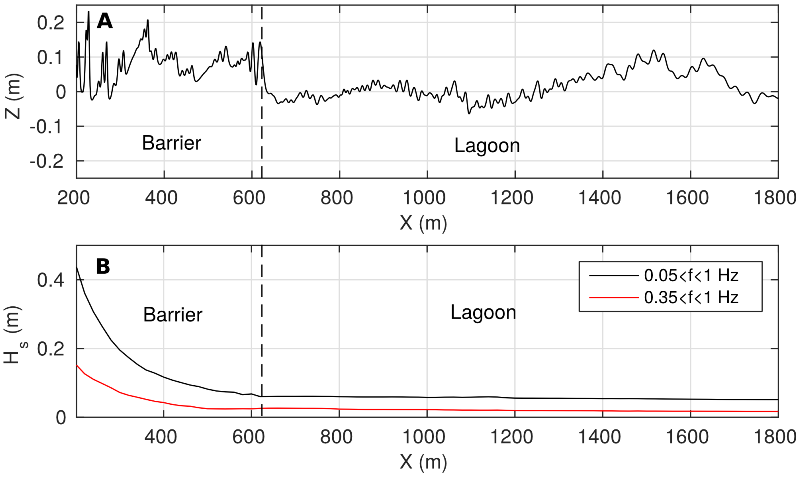

Figure 16: Numerical propagation of undular bores across the barrier (SW10 model). A: free surface elevation. B: cross-shore profiles of SW and bores significant wave heights.The vertical dashed line indicates the end of the barrier.

lighted by the comparison between forereef measurements and regional modeling of wave propagation (WW3) performed in Figure 3. Refraction results in a reef-normal wave forcing at the outer boundary of the reef barrier system, which supports the purely cross-shore analysis performed here. The reflection is estimated from local high resolution wave model (SWASH) to be of the order of 1 % in terms of wave energy.

Wave breaking in such sloping and rough environments is in general poorly documented, in particular from in-situ measurements. The observations show that most SW energy is attenuated before the reef crest. Such trend is rather well captured, after calibration, by the non-hydrostatic phase-resolving numerical model SWASH. However, the model, after careful calibration on the SW cross-shore profile and momentum balance, is still not able to accurately represent the IG wave development over the forereef. More specifically, it overestimates IG wave production in the shoaling and breaking zones. A more accurate representation of the complexity of reef roughness and its variability across the barrier could possibly improve the results, but would require a finer parameterization of roughness depending on both water depth and local colony properties. It should also be noted that when the physical roughness height increases to more than few percents of the water depth, which is typically the case above the reef top at low tide, the concept of bottom roughness itself becomes irrelevant and the flow and wave dynamics should be discussed in the framework of porous media [45, 46]. Another possible cause for IG overestimation is the lack of detailed measurements of the incident conditions. The present simulations are forced by synthetic time series reconstructed by the model from simple statistical wave properties H_s and T_p provided by the S4 measurements. Additionally, the modeling approach adopted here is purely cross-shore, which means that wave directional spreading is not of accounted for. The lack of directional spreading is expected to enhance the IG wave forcing and thus increase IG wave energy generation (e.g., [47]).

The IG energy over the reef top is well correlated with the offshore SW energy flux, as observed by Inch et al. [31] for sandy beaches. Such IG fluctuations are then transmitted into the lagoon, with a depth-dependent frictional dissipation, such as the remaining amount of IG energy in the lagoon is clearly dependent of depth: the higher the water level is, the stronger the IG wave energy is. For the stronger wave event recorded, IG significant heights reach up to 0.9 m at CP2 (just before the reef crest). IG waves are therefore expected to be an important driver of the whole lagoon dynamics.

An important feature revealed by the field observations is the presence of VLF oscillations over the barrier that could result from seiching oscillations, i.e. partially standing wave motions attached to the bathymetry. The reef barrier may *a priori* experience several types of seiching oscillations. First, the lagoon can be considered as a basin either closed or semi-open at the reef boundary. In the former case, the expected fundamental seiching wave has a node near the basin center and two anti-nodes at the lagoon boundaries. The oscillation period depends on the water depth and the exact bathymetric profile, but assuming a 12 m deep 6000 m long flat basin, the fundamental frequency is f_0 =9.4.10^{-4} Hz (higher nth harmonics are at nf_0). If the basin is considered semi-open, seiching frequencies are $((2n+1)/2)f_0$. The fundamental mode ($n=0$) shows a node at the reef barrier and an anti-node at the inner lagoon. Second, the reef flat itself shows strong bathymetric gradients at its boundaries inducing discontinuities in the wave celerity which can possibly induce partial reflection of surface waves. Again, the reef standing wave pattern can potentially be forced by partial reflection at one or both barrier boundaries. The reef length should thus match one quarter/one half wave length of the oscillation, respectively. Considering a typical reef length about 500 m and reef-averaged high and low tide depths of 0.7 and 1.8 m, the corresponding seiching frequencies should be about 0.0013 and 0.0021 Hz at low/high tide for the quarter wave length case and 0.0026 and 0.0042Hz for the half wave length case. It is emphasized that seiching oscillations attached to the reef barrier would naturally be more dependent on depth, because relative depth fluctuations are much more important on the reef than in the lagoon. Summarizing, seiching oscillations are expected in this case to have fundamental frequencies between 10^{-4} and 0.005 Hz, which is well below the 0.01 Hz cut-off frequency used in this paper to differentiate VLF from IG waves.

Peaks around 0.0009, 0.0021 and 0.0042 Hz have been consistenly observed in the field measurements, with variable magnitudes depending on wave and tide conditions. Strong reflection has been observed in the VLF band over the reef flat, in particular for the two upper peaks. Similar features have been highlighted by the numerical simulations. The series of idealized cases performed to test the effect of boundaries, both barrier inner boundary and lagoon shoreline, have confirmed that such reflection patterns are controlled by the system geometry. Taken together, these results demonstrate the combined effects of reef and lagoon boundaries on the reflection processes and the generation or amplification of VLF standing wave patterns in the frequency ranges close to those predicted by the simple seiche theory. On one hand, the bathymetric discontinuities at the reef barrier boundaries promote the development of VLF waves in the band 0.0017 - 0.01 Hz. The more pronounced peak at 0.0021 Hz is associated to a quarter wave length pattern indicating partial reflection at reef inner boundary (bathymetric step). A weaker peak around 0.004Hz also suggests the presence of a half-wave length pattern, with reflection at both barrier boundaries. On the other hand, the shore at the inner boundary of the lagoon induces further reflection which produces VLF fluctuations at lower frequencies, about 0.0009 Hz. The VLF features (amplitude and period) are controlled by the incoming wave energy, the water level and the bathymetric features at the scale of the entire reef-lagoon system. It should be noted that the analysis performed here is purely cross-shore, i.e. along-reef components are ignored although they probably play a non-negligible role in the VLF dynamics within the Ouano lagoon. The along-shore dynamics is mainly controlled here by the offshore wave incidence and the wind [25]. This latter imposes a nearly periodic surface shear nearly aligned with the main lagoon axis (see Fig. 3, D and E) which can modify the lagoon circulation. Furthermore, the wind magnitude reached in the afternoon may affect the breaking process and generate an along-shore propagating short-wave field. These mechanisms deserve to be further explored in the future.

Another peculiar feature is the presence of undular bores (whelps) propagating over the backreef, resulting from the destabilization of wave fronts. Their development is controlled by the value of the Froude number, which means that they are dependent on the local water depth governed by the IG waves. Although they are observed in a wide range of conditions over the Ouano reef, these whelps have a rather weak contribution to the wave energy budget. However, their presence may lead to a modification of the skewness and the acceleration near wave fronts and may affect further the agitation inside the lagoon.

The set of results raised by the present paper should be used as a guide for future studies. This calls in particular for high resolution instrumentation over the forereef combined with micro-topography measurements of the reef structure in order to get a better insight on the breaking process and IG wave production. Another topic of importance, which will be explored in a future paper, is the examination of the momentum balance above the reef to characterize the relationship between wave setup, gradients of radiation stress and cross-reef currents.

6. Conclusion

The present paper reports on a two-month long field experiment in the Ouano reef barrier, New Caledonia. The instrumentation was deployed along a single cross-shore transect to study wave transformation from the forereef to the inner lagoon. In addition, a series of numerical simulations were performed to further explain the field observations. The study shows a strong swell wave attenuation across the reef barrier combined with major energy transfer toward lower frequencies in IG and VLF bands. The swell transformation is well reproduced by the wave-resolving SWASH model, although further work is needed to improve the represention of IG wave dynamics over the forereef. The Ouano reef system is further characterized by two main VLF standing wave patterns. The first, around 0.0021 Hz, is attached to the barrier with partial reflection at the barrier inner boundary (quarter-wave length case). The second, around 0.0009 Hz, is associated to fundamental oscillations of the entire reef-lagoon system in the cross-shore axis. At the other end of the wave spectrum, an additional peculiar feature is the presence of undular bore trains propagating across the backreef. Their development is controlled by the individual Froude number of incoming swell waves. However, despite of their remarkable visual signature, these undular bores are observed to carry individually a little part of the wave energy.

Acknowledgments

This study was sponsored by the EC2CO OLZO program (CNRS INSU), the OLZO and CROSS-REEF Action Sud (MIO IRD), the ANR project MORHOC'H (ANR-13-ASTR-0007) and the

CNFC (N/O Alis). The Noumea IRD center and the GLADYS group (www.gladys-littoral.org) supported the experimentation. We are grateful to all the contributors involved in this experiment, in particular to David Varillon (US IMAGO), Eric Folcher and Bertrand Bourgeois (SEOH) whose efforts were essential to the deployment. The authors are particularly indebted to Pascal Douillet for providing free access to bathymetric data and to Laurie Vincent from NortekMed for her technical support.

[1] G. Symonds, K. P. Black, I. R. Young, Wave-driven flow over shallow reefs, Journal of Geophysical Research: Oceans 100 (C2) (1995) 2639–2648.

[2] C. J. Hearn, Wave-breaking hydrodynamics within coral reef systems and the effect of changing relative sea level, Journal of Geophysical Research: Oceans 104 (C12) (1999) 30007–30019.

[3] M. R. Gourlay, G. Colleter, Wave-generated flow on coral reefsan analysis for two-dimensional horizontal reef-tops with steep faces, Coastal Engineering 52 (4) (2005) 353–387.

[4] P. Bonneton, J.-P. Lefebvre, P. Bretel, S. Ouillon, P. Douillet, Tidal modulation of wave-setup and wave-induced currents on the aboré coral reef, new caledonia, J. Coast. Res 50 (2007) 762–766.

[5] R. J. Lowe, J. L. Falter, S. G. Monismith, M. J. Atkinson, Wave-driven circulation of a coastal reef-lagoon system, Journal of Physical Oceanography 39 (4) (2009) 873–893.

[6] C. Chevalier, D. Sous, J.-L. Devenon, M. Pagano, G. Rougier, J. Blanchot, Impact of cross-reef water fluxes on lagoon dynamics: a simple parameterization for coral lagoon circulation model, with application to the ouano lagoon, new caledonia, Ocean Dynamics (2015) 1509–1534doi:10.1007/s10236-015-0879-x.

[7] H. Fernando, J. McCulley, S. Mendis, K. Perera, Coral poaching worsens tsunami destruction in sri lanka, Eos, Transactions American Geophysical Union 86 (33) (2005) 301–304.

[8] M. Gourlay, Wave set-up on coral reefs. 1. set-up and wave-generated flow on an idealised two dimensional horizontal reef, Coastal Engineering 27 (3) (1996) 161–193.

[9] C. Storlazzi, J. Logan, M. Field, Quantitative morphology of a fringing reef tract from high-resolution laser bathymetry: Southern molokai, hawaii, Geological Society of America Bulletin 115 (11) (2003) 1344–1355.

[10] Y. Yao, Z. Huang, S. G. Monismith, E. Y. Lo, Characteristics of monochromatic waves breaking over fringing reefs, Journal of Coastal Research 29 (1) (2012) 94–104.

[11] A. Van Dongeren, R. Lowe, A. Pomeroy, D. M. Trang, D. Roelvink, G. Symonds, R. Ranasinghe, Numerical modeling of low-frequency wave dynamics over a fringing coral reef, Coastal Engineering 73 (2013) 178–190.

[12] S. G. Monismith, L. M. Herdman, S. Ahmerkamp, J. L. Hench, Wave transformation and wave-driven flow across a steep coral reef, Journal of Physical Oceanography 43 (7) (2013) 1356–1379.

[13] O. Nwogu, Z. Demirbilek, Infragravity wave motions and runup over shallow fringing reefs, Journal of waterway, port, coastal, and ocean engineering 136 (6) (2010) 295–305.

[14] V. Roeber, K. F. Cheung, Boussinesq-type model for energetic breaking waves in fringing reef environments, Coastal Engineering 70 (2012) 1–20.

[15] S.-F. Su, G. Ma, Modeling two-dimensional infragravity motions on a fringing reef, Ocean Engineering 153 (2018) 256–267.

[16] A. Pomeroy, R. Lowe, G. Symonds, A. Van Dongeren, C. Moore, The dynamics of infragravity wave transformation over a fringing reef, Journal of Geophysical Research: Oceans 117 (C11022) (2012) 1–17. doi:10.1029/2012JC008310.

[17] A.-C. N. Péquignet, J. M. Becker, M. A. Merrifield, Energy transfer between wind waves and low-frequency oscillations on a fringing reef, i pan, g uam, Journal of Geophysical Research: Oceans 119 (10) (2014) 6709–6724.

[18] X. Bertin, V. D. A. De Bakker Anouk, C. Giovanni, A. Gael, A. Fabrice, B. Philippe, B. Frederic, C. Bruno, C. Crawford Wayne, D. Mark, et al., Infragravity waves: from driving mechanisms to impacts, Earth Science Reviews 177 (2018) 774–799.

[19] A. C. N. Péquignet, J. M. Becker, M. A. Merrifield, J. Aucan, Forcing of resonant modes on a fringing reef during tropical storm man-yi, Geophysical Research Letters 36 (3) (2009) 1–6. doi:10.1029/2008GL036259.

[20] M. Gawehn, A. van Dongeren, A. van Rooijen, C. D. Storlazzi, O. M. Cheriton, A. Reniers, Identification and classification of very low frequency waves on a coral reef flat, Journal of Geophysical Research: Oceans 121 (10) (2016) 7560–7574.

[21] J. Becker, M. Merrifield, M. Ford, Water level effects on breaking wave setup for pacific island fringing reefs, Journal of Geophysical Research: Oceans 119 (2) (2014) 914–932.

[22] O. Vetter, J. M. Becker, M. A. Merrifield, A.-C. Pequignet, J. Aucan, S. J. Boc, C. E. Pollock, Wave setup over a pacific island fringing reef, Journal of Geophysical Research: Oceans 115 (C12) (2010) 1–13. doi:10.1029/2010JC006455.

[23] A.-C. Péquignet, J. Becker, M. Merrifield, S. Boc, The dissipation of wind wave energy across a fringing reef at ipan, guam, Coral Reefs 30 (1) (2011) 71–82.

[24] S. G. Monismith, J. S. Rogers, D. Koweek, R. B. Dunbar, Frictional wave dissipation on a remarkably rough reef, Geophysical Research Letters 42 (10) (2015) 4063–4071.

[25] D. Sous, C. Chevalier, J.-L. Devenon, J. Blanchot, M. Pagano, Circulation patterns in a channel reef-lagoon system, ouano lagoon, new caledonia, Estuarine, Coastal and Shelf Science 196 (2017) 315–330.

[26] F. Locatelli, D. Sous, V. Rey, C. Chevalier, F. Bouchette, J. Touboul, J.-L. Devenon, Wave transformation over the ouano reef barrier, new caledonia, in: Proceedings of Coastal Dynamics 2017, Helsingor, 12-16 june, 2017, pp. 356–367.

[27] D. des Technologies et des Services de l'Information, Atlas bathymtrique de la nouvelle-calédonie - programme zonéco, Tech. rep., Gouvernement de la Nouvelle Calédonie (2009).

[28] N. Rascle, F. Ardhuin, A global wave parameter database for geophysical applications. part 2: Model validation with improved source term parameterization, Ocean Modelling 70 (2013) 174–188.

[29] J. Aucan, M. Vendé-Leclerc, P. Dumas, M. Bricquir, Wave forcing and morphological changes of new caledonia lagoon islets: Insights on their possible relations, Comptes Rendus Geoscience 349 (6) (2017) 248–259.

[30] D. Drevard, V. Rey, P. Fraunié, Partially standing wave measurement in the presence of steady current by use of coincident velocity and/or pressure data, Coastal Engineering 56 (9) (2009) 992–1001.

[31] H. Chanson, Current knowledge in hydraulic jumps and related phenomena. a survey of experimental results, European Journal of Mechanics-B/Fluids 28 (2) (2009) 191–210.

[32] D. Peregrine, Calculations of the development of an undular bore, Journal of Fluid Mechanics 25 (2) (1966) 321–330.

[33] P. A. Madsen, D. R. Fuhrman, H. A. Schäffer, On the solitary wave paradigm for tsunamis, Journal of Geophysical Research: Oceans 113 (C12) (2008) 1–22. doi:10.1029/2008JC004932.

[34] G. El, R. Grimshaw, A. Kamchatnov, Evolution of solitary waves and undular bores in shallow-water flows over a gradual slope with bottom friction, Journal of Fluid Mechanics 585 (2007) 213–244.

[35] J.-F. Filipot, K. F. Cheung, Spectral wave modeling in fringing reef environments, Coastal Engineering 67 (2012) 67–79.

[36] R. K. Hoeke, C. D. Storlazzi, P. V. Ridd, Drivers of circulation in a fringing coral reef embayment: a wave-flow coupled numerical modeling study of hanalei bay, hawaii, Continental Shelf Research 58 (2013) 79–95.

[37] M. Buckley, R. Lowe, J. Hansen, Evaluation of nearshore wave models in steep reef environments, Ocean Dynamics 64 (6) (2014) 847–862.

[38] M. Zijlema, Modelling wave transformation across a fringing reef using swash, Coastal Engineering Proceedings 1 (33) (2012) 26.

[39] C. H. Lashley, D. Roelvink, A. van Dongeren, M. L. Buckley, R. J. Lowe, Nonhydrostatic and surfbeat model predictions of extreme wave run-up in fringing reef environments, Coastal Engineering 137 (2018) 11–27.

[40] M. Zijlema, G. Stelling, P. Smit, Swash: An operational public domain code for simulating wave fields and rapidly varied flows in coastal waters, Coastal Engineering 58 (10) (2011) 992–1012.

[41] K. Hasselmann, On the non-linear energy transfer in a gravity-wave spectrum part 1. general theory, Journal of Fluid Mechanics 12 (4) (1962) 481–500.

[42] D. P. Rijnsdorp, G. Ruessink, M. Zijlema, Infragravity-wave dynamics in a barred coastal region, a numerical study, Journal of Geophysical Research: Oceans 120 (6) (2015) 4068–4089.

[43] M. L. Buckley, R. J. Lowe, J. E. Hansen, A. R. Van Dongeren, Wave setup over a fringing reef with large bottom roughness, Journal of Physical Oceanography 46 (8) (2016) 2317–2333.

[44] S. G. Monismith, Flow through a rough, shallow reef, Coral Reefs 33 (1) (2014) 99–104.

[45] G. Arnaud, V. Rey, J. Touboul, D. Sous, B. Molin, F. Gouaud, Wave propagation through dense vertical cylinder arrays: Interference process and specific surface effects on damping, Applied Ocean Research 65 (2017) 229–237.

[46] D. Roelvink, R. McCall, S. Mehvar, K. Nederhoff, A. Dastgheib, Improving predictions of swash dynamics in xbeach: The role of groupiness and incident-band runup, Coastal Engineering 134 (2018) 103 – 123, rISC-KIT: Resilience-increasing Strategies for Coasts Toolkit. doi:https://doi.org/10.1016/j.coastaleng.2017.07.004.
URL `http://www.sciencedirect.com/science/article/pii/S0378383917301321`

[47] K. Inch, M. Davidson, G. Masselink, P. Russell, Observations of nearshore infragravity wave dynamics under high energy swell and wind-wave conditions, Continental Shelf Research 138 (2017) 19–31.

CASE	**RESULTS**																	
	Offshore		CP2			CP3			CP4			CP5			Sig		CP6	
	H_o	H_a	H_s^{sw}	H_s^{ig}	MWL	H_s^{sw}	H_s^{ig}	MWL	H_s^{sw}	H_s^{ig}	MWL	H_s^{sw}	H_s^{ig}	MWL	H_s^{sw}	H_s^{ig}	H_s^{sw}	H_s^{ig}
	(m)	(m)	(m)	(m)	(m)	(m)	(m)	(m)	(m)	(m)	(m)	(m)	(m)	(m)	(m)	(m)	(m)	(m)
	Reference Case																	
Ref. Meas.	2.44	-	0.65	0.32	0.44	0.37	0.26	0.5	0.26	0.25	0.44	0.14	0.19	0.38	0.14	0.11	0.08	0.12
RefSW2	-	2.4	0.64	0.4	0.42	0.4	0.34	0.4	0.24	0.31	0.37	0.12	0.23	0.34	0.03	0.16	0.03	0.1
RefSW10	-	2.4	0.65	0.41	0.41	0.44	0.39	0.42	0.31	0.36	0.41	0.19	0.32	0.38	0.09	0.21	0.07	0.14
	Additional cases																	
A1 Meas.	2.44	-	0.81	0.33	0.67	0.52	0.29	0.73	0.37	0.29	0.68	0.21	0.24	0.63	0.21	0.16	0.14	0.15
A1SW2	-	2.4	0.74	0.4	0.63	0.48	0.35	0.62	0.32	0.32	0.6	0.17	0.26	0.56	0.05	0.17	0.05	0.11
A2 Meas.	2.43	-	0.54	0.3	0.19	0.26	0.21	0.26	0.17	0.21	0.18	0.09	0.14	0.1	0.08	0.06	0.06	0.06
A2SW2	-	2.4	0.53	0.4	0.14	0.29	0.3	0.11	0.17	0.21	0.07	0.08	0.19	0.05	0.02	0.13	0.01	0.07
B1 Meas.	3.96	-	1.27	0.73	1	1.06	0.69	1.01	0.78	0.66	1.03	0.52	0.58	0.98	-	-	0.24	0.43
B1SW2	-	5.1	1.19	0.92	1.03	0.8	0.79	0.98	0.54	0.67	0.94	0.32	0.51	0.88	-	-	0.07	0.26
B2 Meas.	3.85	-	0.97	0.61	0.54	0.63	0.51	0.62	0.49	0.5	0.55	0.31	0.42	0.47	-	-	0.15	0.24
B2SW2	-	5.2	0.94	0.88	0.66	0.59	0.71	0.61	0.38	0.56	0.56	0.21	0.36	0.44	-	-	0.05	0.19
C1 Meas.	1.11	-	0.61	0.17	0.66	0.43	0.17	0.71	0.32	0.18	0.69	0.23	0.14	0.66	-	-	0.12	0.11
C1SW2	-	1.1	0.69	0.19	0.67	0.49	0.18	0.68	0.37	0.16	0.69	0.26	0.13	0.68	-	-	0.15	0.06
C2 Meas.	1.26	-	0.25	0.18	-0.19	0.07	0.09	-0.15	0.01	0.03	-0.23	0	0.01	-0.3	-	-	0.015	0
C2SW2	-	1.3	0.3	0.2	-0.21	0.12	0.16	-0.22	0.06	0.13	-0.26	0.04	0.07	-0.31	-	-	0.06	0.02
SW2 Mean Err. (%)	-	-	8.8	24.6	11.6	22.6	33.4	21.3	97	61.3	16.7	24.5	112	14	75.6	61.4	101.7	41.5

Table 2: Additional cases: comparison between model prediction and experimental results. The Mean Error is the mean of the absolute values of relative errors.